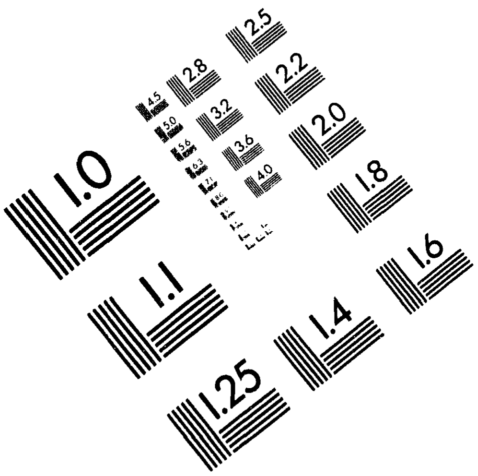

AIIM

Association for Information and Image Management

1100 Wayne Avenue, Suite 1100
Silver Spring, Maryland 20910
301/587-8202

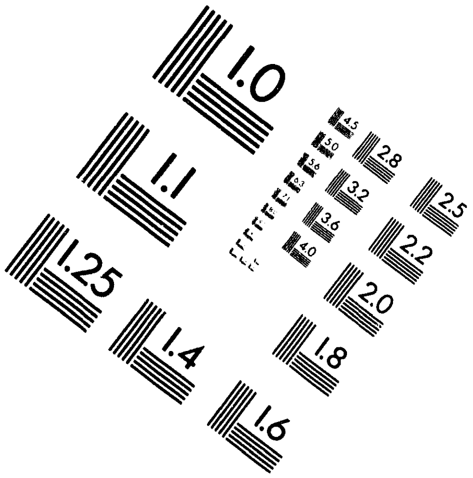

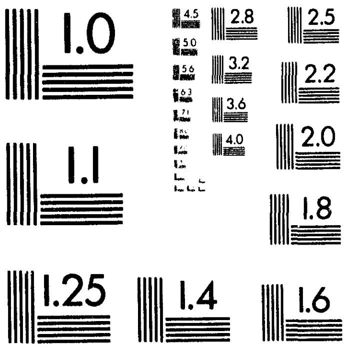

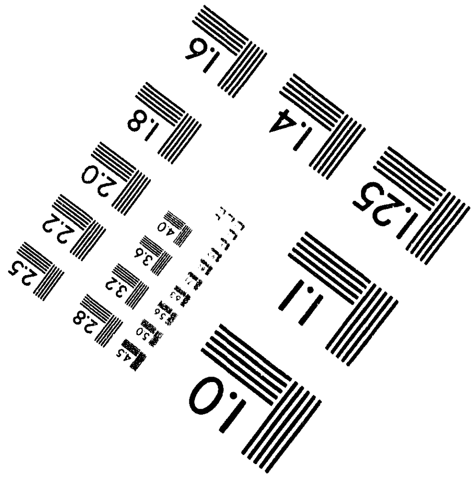

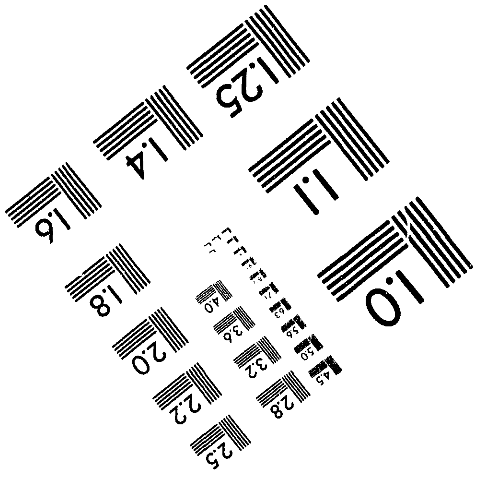

MANUFACTURED TO AIIM STANDARDS
BY APPLIED IMAGE, INC.

1 of 1

Conf-940723--13

UCRL-JC-116340
PREPRINT

Three-Dimensional Ground Penetrating Radar Imaging Using Multi-Frequency Diffraction Tomography

Jeffrey E. Mast
Erik M. Johansson

This paper was prepared for submittal to:
SPIE 1994 International Symposium on Optics,
Imaging and Instrumentation
San Diego, California, USA
July 24 - 29, 1994

July 1994

Lawrence Livermore National Laboratory

Three-dimensional ground penetrating radar imaging using multi-frequency diffraction tomography

Jeffrey E. Mast and Erik M. Johansson

Lawrence Livermore National Laboratory
PO Box 808, L-153
Livermore, CA 94550

ABSTRACT

In this paper we present results from a three-dimensional image reconstruction algorithm for impulse radar operating in monostatic pulse-echo mode. The application of interest to us is the nondestructive evaluation of civil structures such as bridge decks. We use a multi-frequency diffraction tomography imaging technique in which coherent backward propagations of the received reflected wavefield form a spatial image of the scattering interfaces within the region of interest. This imaging technique provides high-resolution range and azimuthal visualization of the subsurface region. We incorporate the ability to image in planarly layered conductive media and apply the algorithm to experimental data from an offset radar system in which the radar antenna is not directly coupled to the surface of the region. We present a rendering in three-dimensions of the resulting image data which provides high-detail visualization.

Keywords: diffraction tomography, inverse scattering, holography, migration, ground penetrating radar, impulse radar, radar imaging, synthetic aperture radar

1. INTRODUCTION

Ground penetrating radar (GPR) has been used for many applications including locating hazardous wastes, imaging of the profile of lake bottoms, and determining characteristics of geological interfaces. Past research involving this pulse-echo technique has included development of the radar system and data processing methods to aid in determining the characteristics of many subsurface regions[1–5]. We are interested in using ground penetrating pulse-echo radar to form a spatial image of the interior of civil structures made of concrete, such as bridge decks, to aid in determining the integrity of the structure. For this application, we are also interested in an offset radar system in which the antenna is not coupled to the surface. The offset is necessary to make it feasible to mount the system on a reasonably fast moving vehicle.

We preprocess the acquired data using several standard techniques to improve the results. The preprocessing includes background subtraction which removes the front surface reflection. We also utilize pulse deconvolution to attain improved signal-to-noise and resolution. The image formation algorithm we present in this paper is based on a multi-frequency diffraction tomography method. The unprocessed data are a collection of time delayed reflections of the GPR impulse from subsurface dielectric interfaces. The imaging algorithm maps these reflections into a high-resolution spatial image of the scattering interfaces.

The imaging method we employ maintains linearity by applying the Born approximation for weak scattering. Based on this approximation we develop the plane-to-plane backward propagation method and extend the imaging method to incorporate planar layers. We emphasize a non-coupled radar which is offset parallel to the surface of the concrete and discuss the theoretical resolution limits of the imaging system with the offset geometry. A reconstruction demonstrating an implementation of the algorithm in three-dimensions is shown rendered for visualization.

2. IMAGING GEOMETRY

We consider two imaging geometries using the first as a basis for providing an imaging method for the second. The first geometry consists of a synthetically formed two-dimensional monostatic planar array of antennas coupled to the surface of a three-dimensional object region as shown in Figure 1 (a). The antenna is operating in pulse-echo mode and has a bandwidth, B, centered about f_o. Each temporal frequency, f, of the pulse corresponds to a different illuminating wavelength, λ, via the

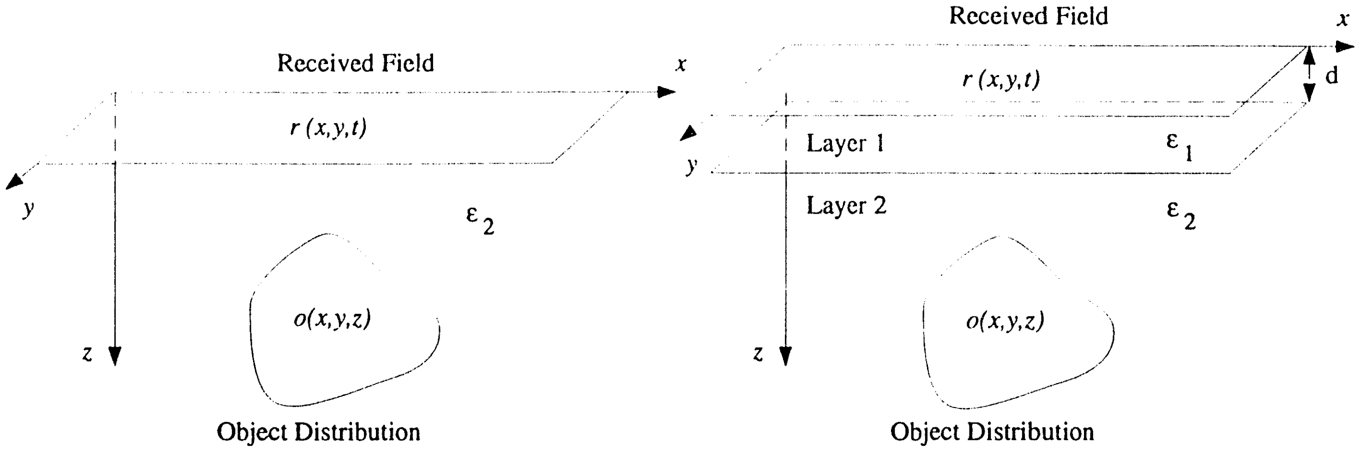

(a)

(b)

Figure 1. Imaging geometry for (a) a coupled antenna array, (b) an offset antenna array. ϵ_1 and ϵ_2 are the permittivities of the layers.

relationship $\lambda = \frac{v}{f}$ where v is the propagation velocity of the medium. The object region consists of a homogeneous medium containing an unknown object distribution $o(x, y, z)$.

In determining the received wavefield at the antenna array for a given wavelength, we make the assumption that the scattering from the object obeys the Born approximation for week scattering[6]. Inherent in this assumption is that the medium between the scattering object and the antenna is homogenous. This approximation linearizes the scattering problem and gives the following relationship between the transmitted wavefield, u, at a given wavelength, the object distribution, and the received wavefield, r,

$$r(x, y; \lambda) = \int [o(x, y, z'; \lambda)u(x, y, z'; \lambda)] * *g(x, y, z'; \lambda)\, dz', \tag{1}$$

where g is the Green's function and $**$ denotes convolution. The Green's function for a homogenous background material is given by

$$g(x, y, z; \lambda) = \frac{e^{jkr}}{4\pi r}, \tag{2}$$

where $r = \sqrt{x^2 + y^2 + z^2}$ and $k = \frac{2\pi}{\lambda}$. The term in square brackets of Equation (1) is the equivalent source of the scattering wavefield that we will denote as s. Under monostatic illumination with an isotropic radiator, the received wavefield becomes

$$r(x, y; \lambda) = \int o(x, y, z') * *g^2(x, y, z'; \lambda)\, dz'. \tag{3}$$

The second geometry is similar to the first, except the antenna array is offset parallel to the surface of the medium by a distance, d, as shown in Figure 1 (b). This geometry represents a non-coupled antenna array when the layer between the antenna array and the object medium is air. We will utilize the assumptions made for the first geometry in solving for the object distribution for this geometry.

3. IMAGING METHOD

In conventional diffraction tomography the tomographic nature of the data is obtained from rotation of the object. For synthetic aperture pulse-echo radar the tomographic information is obtained from the wideband pulse which provides multiple illuminating wavelengths. Each wavelength in the received wavefield represents a different portion of the spectrum of the object distribution. Superimposing the spectral components from each wavelength and then inverse Fourier transforming results in an estimate of the object distribution.

To implement this concept we use the plane-to-plane backward propagation method. Each wavelength of the received wavefield is plane-to-plane backward propagated into the object region and then superimposed. Multiple layer reconstruction is attained by applying boundary conditions at the layer interfaces.

3.1 Wavefield backward propagation

The plane-to-plane backward propagation method models the wave propagation as a spatial linear filter and provides a solution for the equivalent source s in Equation (1) by inverting the nonzero components of the spatial filter. The spatial filter is given as

$$H(f_x, f_y, z; \lambda) = \begin{cases} e^{j2\pi z\sqrt{\frac{1}{\lambda^2} - f_x^2 - f_y^2}}, & f_x^2 + f_y^2 = \frac{1}{\lambda^2}, \\ 0, & otherwise \end{cases} \tag{4}$$

where f_x and f_y denote spatial frequencies in the x and y direction, respectively[7]. Thus, we have that the spatial spectrum of the equivalent source is given by

$$\hat{S}(f_x, f_y, z) = \int R(f_x, f_y; \lambda) H^{\dagger}(f_x, f_y, z; \lambda)\, d\lambda, \tag{5}$$

where R is the spectrum of the received wavefield, and $\dagger$ denotes the pseudo inverse[5]. The estimate of the source distribution is then given by the inverse two-dimensional Fourier transform of $\hat{S}$. Note that each z-plane of the source distribution can be reconstructed independently and hence is referred to as plane-to-plane wavefield backward propagation.

3.2 Monostatic imaging

The goal of this section is to form an inverse solution in the context of backward propagation for the two monostatic geometries discussed earlier. We consider three background media: homogenous, planarly layered, and conductive.

3.2.1 Homogeneous background

In order to represent Equation (3) in a form suitable for solution using the backward propagation method, we must remove the dependency upon g^2. This dependency is removed by taking the derivative of Equation (3) with respect to k resulting in

$$\tilde{r}(x, y; \lambda) = \frac{\partial}{\partial k} r(x, y; \lambda) = C \int o(x, y, z') **g\left(x, y, z'; \frac{\lambda}{2}\right) dz', \tag{6}$$

where C is a constant[8]. Now $\tilde{r}$ is in the form of Equation (1) where the object distribution is considered the source distribution and backward propagation can be applied to reconstruct the object distribution. However, because g is evaluated at $\frac{\lambda}{2}$ instead of λ, the backward propagation filter, H, is also evaluated at $\frac{\lambda}{2}$. Note that the derivative with respect to k is equivalent to removing the loss due to spherical expansion of the incident wavefield. This compensation is generally performed in the preprocessing. A block diagram of the method used to reconstruct the object distribution for a single wavelength is shown in Figure 2. Under multiple wavelength illumination, estimates of the object distribution from each of the wavelengths are sumperimposed.

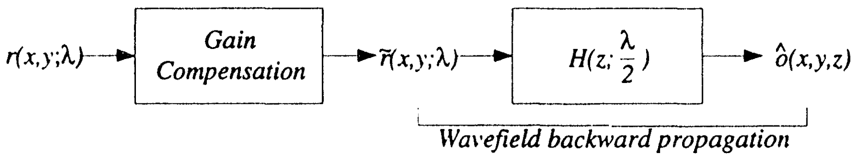

Figure 2. Block diagram depicting reconstruction method for single wavelength monostatic illumination with a homogeneous background

3.2.2 Planarly layered background

We extend the backward propagation model to incorporate a planarly layered background medium as depicted in Figure 1 (b). First, the wavefield at the boundary of the two layers is computed using backward propagation. Then boundary conditions applied at the interface between the two layers allow us to backward propagate the wavefield at the boundary into the second layer using the appropriate spatial filter for that layer.

The constraint applied at the boundary between the two layers is the continuity across the boundary of the f_x and f_y spatial frequency components of the incident wavefield. Figure 3 shows the constraint pictorially in two dimensions. This boundary condition implies that the wavefield in the second layer at the interface equals the wavefield at the boundary in the first layer. However, the wavefield propagation in the second layer is now dependent upon a different dispersion relation and the backward propagation filter now uses the wavelength in the second layer. Figure 4 shows a block diagram of the two-layered backward propagation algorithm for monostatic illumination. We use this algorithm to handle the air layer between the antenna and the surface of the concrete. Note that this method can easily be extended to handle media containing more than two layers.

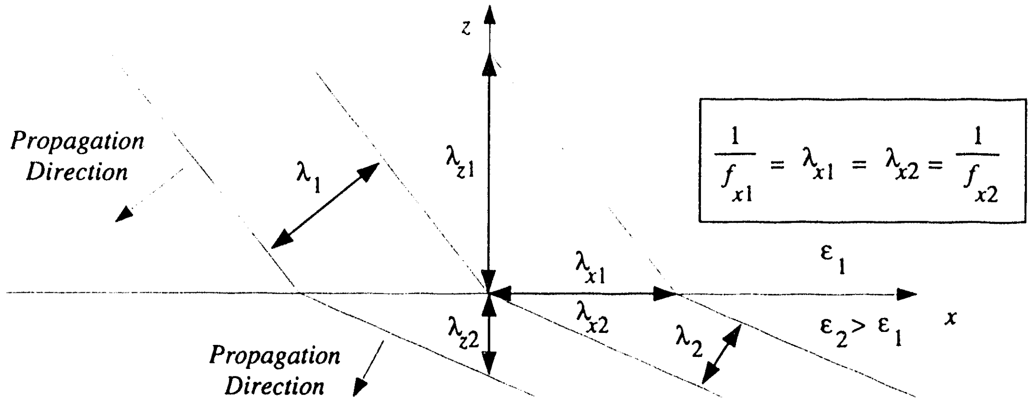

Figure 3. Boundary condition applied at the interface between two layers.

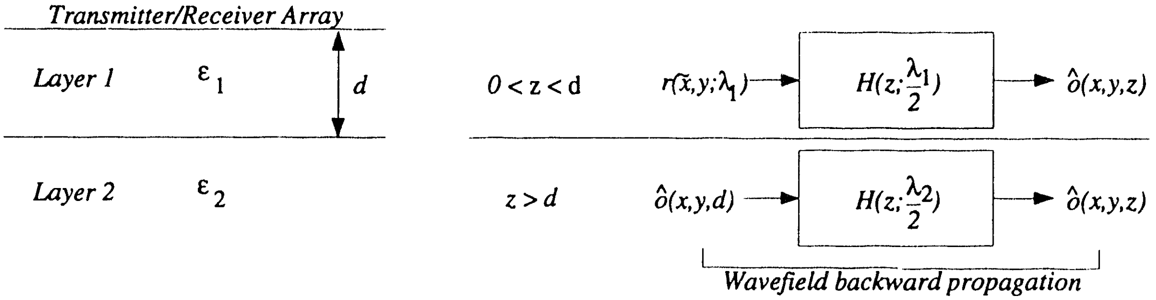

Figure 4. Block diagram depicting reconstruction method for single wavelength monostatic illumination with a layered background.

3.2.3 Conductive background

We can also incorporate conductivity into the backward propagation method. This concept is important because concrete is a conductive medium having a complex permittivity $\bar{\epsilon} = \epsilon'(f)+j\epsilon''(f)$ in which $\bar{k} = 2\pi f\sqrt{\mu\bar{\epsilon}(f)}$. Using $\bar{k}$ in Equation (2) we can solve for a lossy spatial wave propagation filter, $\bar{H}$, which incorporates dispersion and attenuation due to the conductivity. This filter will properly compensate for dispersion; however, the received wavefield contains superpositions of temporal frequency components of pulse echoes from different depths. Therefore, amplification of highly attenuated frequency components will also amplify the frequency components that were not attenuated. Hence, it is necessary to incorporate attenuation compensation into the gain compensation of the preprocessing and make $|\bar{H}| = 1$.

3.3 Resolution limits

The resolution attained in the reconstructed image is dependent upon several factors including frequency bandwidth, antenna beamwidth, distance from the antenna, and medium parameters. To approach the theoretical resolution limits using the described imaging method, the antenna positions must be spaced by at most the cross-range resolution limit.

The range resolution is dependent only upon the propagation velocity of the medium and the pulse bandwidth and is given by

$$\Delta R_z = \frac{v}{2B}. \tag{7}$$

For a single layered medium, the cross-range resolution limit for a synthetic aperture radar is approximately

$$\Delta R_x = \max\left(\frac{\lambda_{\min}}{2}, \frac{\lambda_{\min}}{2\tan\left(\frac{\theta_a}{2}\right)}\right), \tag{8}$$

where $\lambda_{\min}$ is the minimum propagating wavelength and θ_a is the antenna beamwidth[5, 9, 10]. This limit is pictorially shown in Figure 5 (a). Note that the effective length of the synthetic aperture is limited by the beamwidth of the antenna. For a two layered medium, the cross-range resolution limit is computed based on an effective aperture at the interface between the two layers (see Figure 5 (b)). The cross-range resolution limit in the second layer becomes

$$\Delta R_x = \max\left(\frac{\lambda_{\min}}{2}, \frac{\lambda_{\min}}{2\tan\left(\frac{\theta_b}{2}\right)}\right), \tag{9}$$

where θ_b is found based on θ_a and Snell's law at the interface. It is important to note that these resolution limits are for a synthetic array which is only acting as a receiver (such as given by Equation (1)). Based on Equation (6), the cross range resolution limits for a monostatic transmitter/receiver array will improve by a factor of two due to the Green's function being a function of $\frac{\lambda}{2}$.

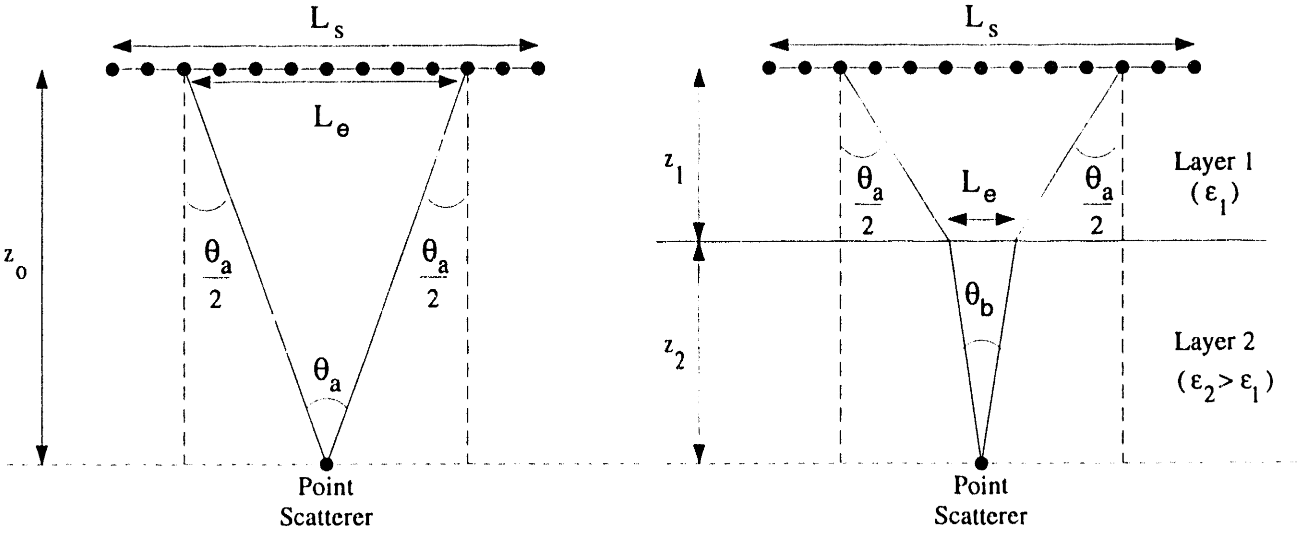

(a) (b)

Figure 5. Relationships between antenna array length and antenna beamwidth for (a) a homogeneous medium and (b) a two-layered medium. L_s denotes the length of the synthetic array and L_e denotes the effective length of the synthetic array given an antenna beamwidth of θ_a.

4. EXPERIMENTAL ANALYSIS

We present results from a ground penetrating radar imaging experiment on a concrete slab. These results demonstrate the capability of the algorithm to produce high resolution images from GPR data using an offset monostatic synthetic array having a geometry similar to that shown in Figure 1 (b).

The experiment consisted of illuminating a concrete slab in monostatic mode using an antenna offset from the concrete surface. A three-dimensional spatial image of the interior of the concrete structure was produced using the multi-layer imaging algorithm described in this paper. Three-dimensional rendering and planar slicing of this image provide a means for visualizing the results.

4.1 The concrete test bed

The test bed, shown in Figure 6 before pouring the concrete, contains reinforcing bars, both fixed and removable, and other objects designed to provide a method for evaluating data acquisition and imaging performance. The concrete slab is approximately 1.8 m square and is 30 cm thick. The objects are meant to emulate spawling, delaminations, and voids in the concrete. Two teflon cylindrical objects simulate spawling and three small hollow plastic spheres simulate voids. Two square teflon plates simulate delaminations and the PVC pipes contain removable reinforcing bars (rebars). Toward the bottom of the slab is a grid of rebars separated by 25 cm. The depths of the objects range from 6 cm to 25 cm.

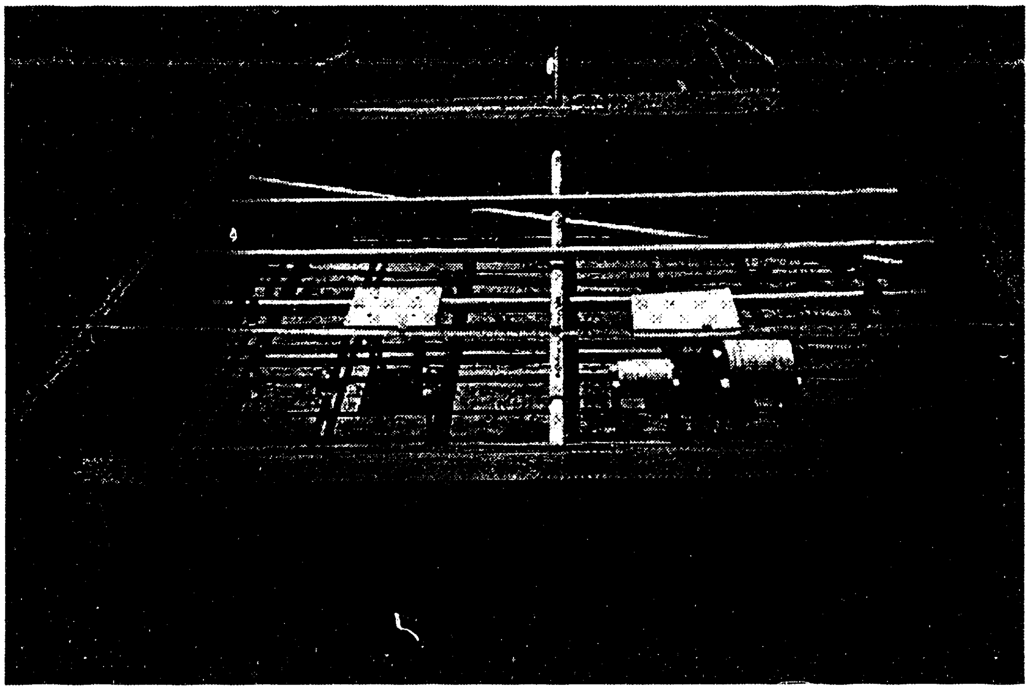

Figure 6. Test bed prior to concrete pour.

4.2 Data acquisition

The data acquisition procedure consisted of monostatic illumination of the top surface of the concrete slab using a horn antenna with an approximate beamwidth of 60°. We used a relatively low power pulser (~ 1 Watt peak) to provide the excitation for the antenna. The low power limited our depth of penetration in conjunction with the attenuation in the concrete and the surface reflection. This system produced a signal having frequency content from approximately 1.2 GHz to 3.5 GHz. We synthesized a 1.5 m square aperture with 1.27 cm sample spacing. For this particular experiment we intended to test the capabilities of a non-coupled antenna and used a gap of approximately 7.5 cm between the antenna and the surface of the concrete.

4.3 Imaging results

We processed the data obtained from the slab using a relative permittivity of 9 which we computed experimentally. The dispersiveness of the concrete did not appear to be much of a factor; however, there was a large amount of attenuation. The results from imaging are shown in Figures 7 and 8. We provide two means for visualizing the generated three-dimensional image – planar slicing and three-dimensional rendering. Planar slicing is a simple technique for visualizing portions of the data for making positional measurements However, three-dimensional rendering gives an overall perspective of object orientation and shape within the image. Figures 7 (a) and (b) are planar slices of the reconstructed image. A rendered version of the image is shown in Figure 8.

Four rebars are visible in the rendered image. The slanted rebar is only visible at shallower depths mainly due to shadowing by the rebars crossing over it and due to limited signal penetration depth. The particular colormap and scaling chosen for this

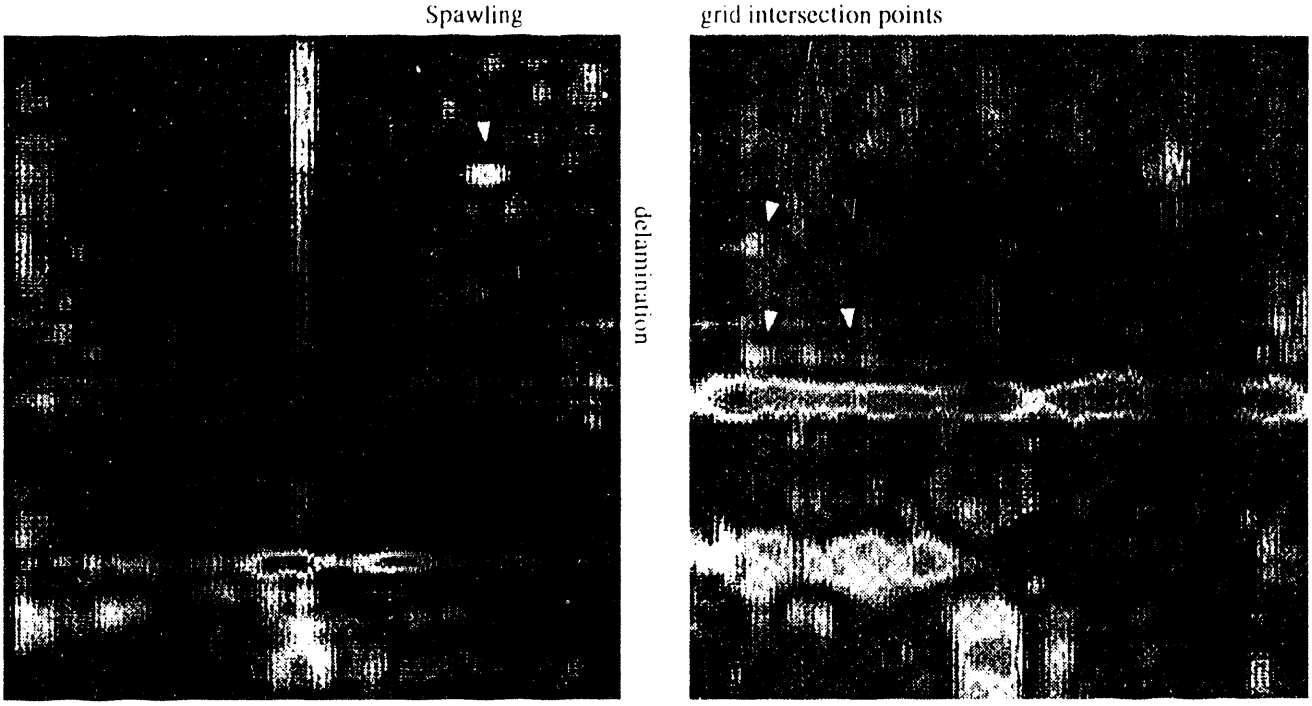

(a) (b)

Figure 7. Planar slice of the 3D image of the concrete test bed at a depth of (a) 14 cm and (b) 24 cm. Spawling and delamination anomalies are visible in (a) and the intersections of the rebar grid are visible in (b).

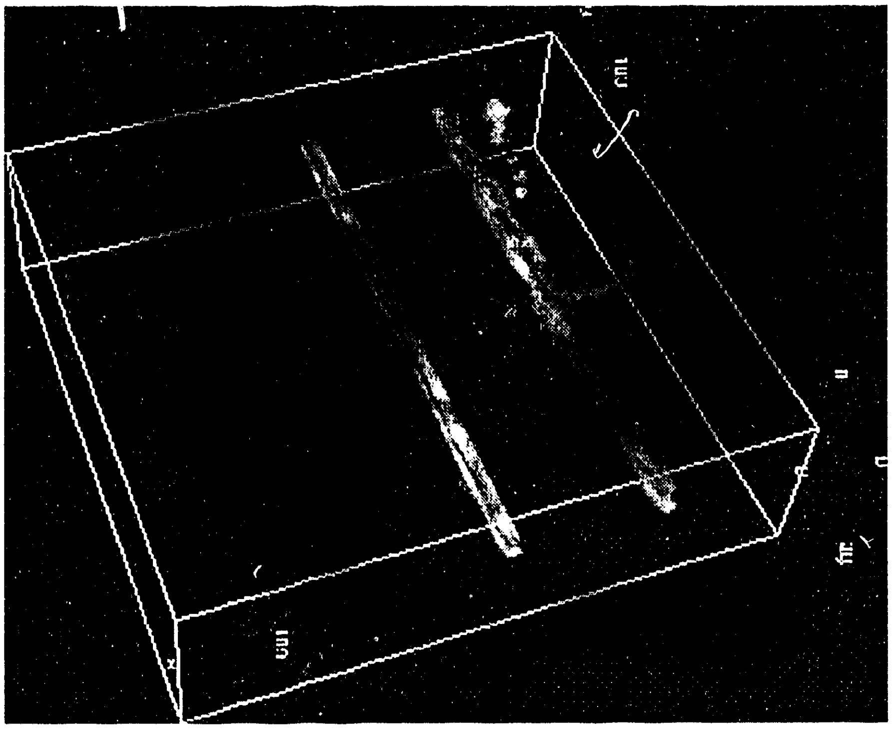

Figure 8. Three-dimensional rendered image of the interior structure of the concrete test bed. Four rebars are visible as well as the spawling anomaly.

rendering does not allow for three-dimensional visualization of any of the other objects. To visualize those, we use planar slices. Figure 7 (a) and (b) show planar slices of the slab at depths of 14 and 24 cm, respectively. Note in Figure 7 (a) the large spawling anomaly is visible in the upper left corner. The spherical voids are not discernible in the reconstruction most likely due to background clutter and their small scattering surface. However, the delamination anomalies are discernible and one of them is shown in Figure 7 (a). The lower rebar grid is visible in Figure 7 (b). The intersection points in the grid were strong scattering centers and are pointed out in the Figure.

5. CONCLUSIONS

We have demonstrated the imaging of the interior structure of a concrete slab using a non-coupled pulsed microwave data acquisition system. The imaging method is based upon multi-frequency diffraction tomography utilizing plane-to-plane backward propagation to account for multiple layered media. The offset of the antenna from the concrete places severe constraints on the resulting resolution and detection capabilities of the imaging system. In particular, the system we used was limited by the low power of the pulser due to the significant amount of attenuation in the concrete as well as the large loss due to the reflection at the air/concrete interface. However, we can obtain deeper penetration depths by increasing the power of the pulser and utilizing lower frequencies between 100 MHz and 1 GHz. In spite of the limitations of an offset antenna array, the data acquisition and subsequent imaging did provide accurate visualization of several subsurface anomalies in the concrete.

6. ACKNOWLEDGMENTS

The authors would like to thank the other members the GPIR project team who have helped make this work possible: John Warhus for his project leadership and pulser work; and Scott Nelson for preforming electromagnetic modelling and aiding in the data acquisition and visualization.

This work was performed under the auspices of the U.S. Department of Energy by Lawrence Livermore National Laboratory under contract No. W-7405-Eng-48.

7. REFERENCES

1. D. J. Daniels, D. J. Gunton, and H. F. Scott, "Introduction to subsurface radar," *IEE Proceedings on Communications, Radar, and Signal Processing*, vol. 135, Pt. F, pp. 278–320, Aug. 1988.
2. Y. Michiguchi, K. Hiramoto, M. Nishi, Toshihide, and M. Okada, "Advanced subsurface radar system for imaging buried pipes," *IEEE Transactions on Geosience and Remote Sensing*, vol. 26, pp. 733–740, Nov. 1988.
3. G. Junkin and A. P. Anderson, "Limitations in microwave holographic synthetic aperture imaging over a lossy half-space," *IEE Proceedings on Communications, Radar, and Signal Processing*, vol. 135, Pt. F, pp. 321–329, Aug. 1988.
4. N. Osumi and K. Ueno, "Microwave holographic imaging method with improved resolution," *IEEE Transactions on Antennas and Propagation*, vol. AP-32, pp. 1018–1026, Oct. 1984.
5. J. Mast, *Microwave Pulse-Echo Radar Imaging for the Nondestructive Evaluation of Civil Structures*. PhD thesis, University of Illinois at Urbana-Champaign, 1993.
6. M. Born and E. Wolf, *Principles of Optics*. New York: Pergamon Press, 6th ed., 1980.
7. J. W. Goodman, *Introduction to Fourier Optics*. New York: McGraw-Hill, 1968.
8. S. J. Norton and M. Linzer, "Ultrasonic reflectivity imaging in three dimensions: exact inverse scattering solutions for plane, cylindrical, and spherical apertures," *Proceedings of the IEEE Transactions on Biomedical Engineering*, vol. 28, pp. 202–220, 1981.
9. M. I. Skolnik, *Introduction to Radar Systems*. New York: McGraw-Hill, 2nd ed., 1980.
10. C. Elachi, *Introduction to the Physics and Techniques of Remote Sensing*. New York: John Wiley and Sons, Inc., 1987.

DATE FILMED

9/29/94

END